Volume 202 June 2013 ISSN 0022-4596

ELSEVIER

JOURNAL OF SOLID STATE CHEMISTRY

IN THIS ISSUE:

X-ray absorption spectroscopy study of parent misfit-layered cobalt oxide $[Sr_2O_2]_qCoO_2$

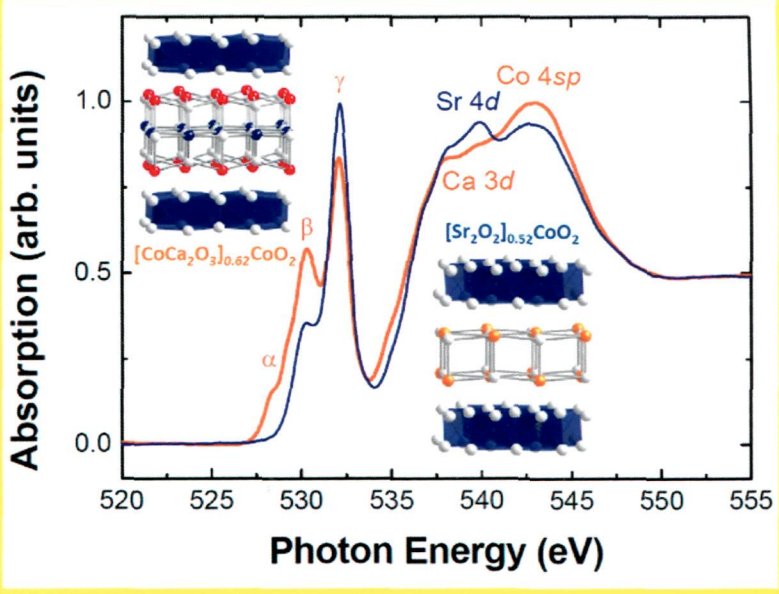

Ta-Lei Chou, Ting-Shan Chan, Jin-Ming Chen,
Hisao Yamauchi and Maarit Karppinen

ELSEVIER

Volume 202, June 2013

JOURNAL OF SOLID STATE CHEMISTRY

www.elsevier.com/locate/jssc

CONTENTS

Abstracted/indexed in BioEngineering Abstracts, Chemical Abstracts, Coal Abstracts, Current Contents/Physics, Chemical, & Earth Sciences, Engineering Index, Research Alert, SCISEARCH, Science Abstracts, and Science Citation Index. Also covered in the abstract and citation database SciVerse SCOPUS®. Full text available on SciVerse ScienceDirect®.

Regular Articles

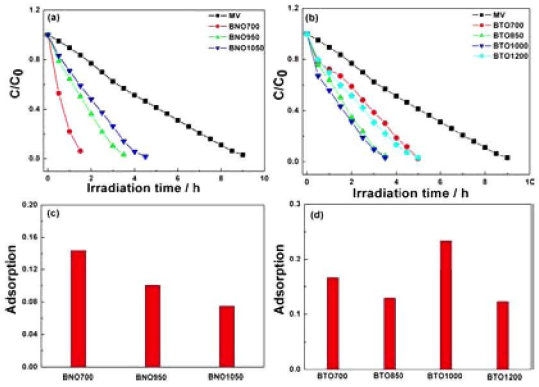

Photodegradation performance and adsorption ability of $BiNbO_4$ and $BiTaO_4$ powders, respectively. BNO700 with the best photocatalytic efficiency is ascribed to its large surface area and more positive conduction band level.

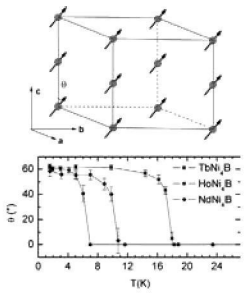

Simplified magnetic structure in $NdNi_4B$ and full magnetic structure in RNi_4B (R = Tb, Ho). Variation with temperature of the easy magnetization axis direction (angle with c-axis) showing a spin re-orientation.

Regular Articles—Continued

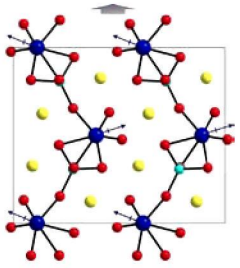

A net moment arising from the alignment of the distorted VO_6 octahedra is responsible for the SHG and piezoelectricity for the noncentrosymmetric vanadium phosphate, Li_2VPO_6.

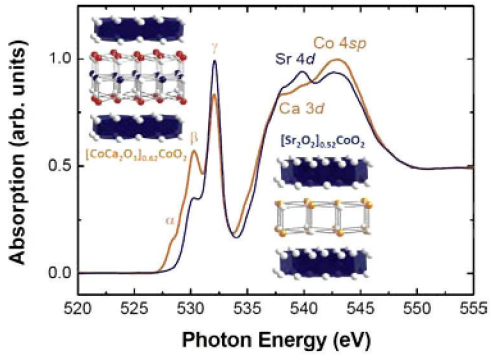

$[Sr_2O_2]_{0.52}CoO_2$ obtained through high-pressure synthesis is a parent of misfit-layered cobalt oxides,such as $[CoCa_2O_3]_{0.62}CoO_2$ or $[M_mA_2O_{2+m}]_qCoO_2$ in general. Our comprehensive X-ray absorption spectroscopy study shows that both $[Sr_2O_2]_{0.52}CoO_2$ and $[CoCa_2O_3]_{0.62}CoO_2$ possess mixed III/IV valence cobalt, but the average Co-valence is a little lower in the former. This is tentatively believed to be due to OH^- groups replacing part of O^{2-} ions in the $[Sr_2O_2]$ layer block.

Continued

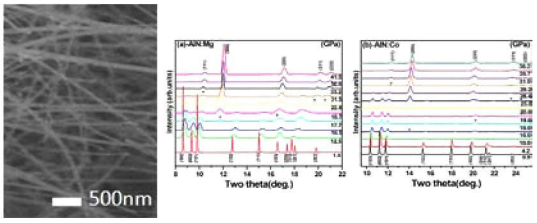

The high-pressure behaviors of AlN:Mg and AlN:Co nanowires have been investigated by *in situ* angle dispersive synchrotron X-ray diffraction.

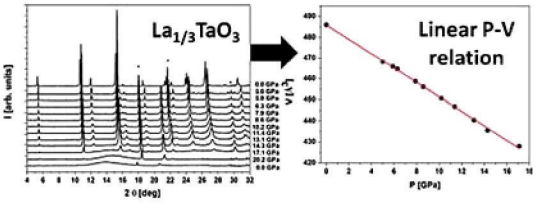

$La_{1/3}Tao_3$ exhibits linear pressure-volume relation until irreversible pressure induced amorphization at18.5 Gpa.

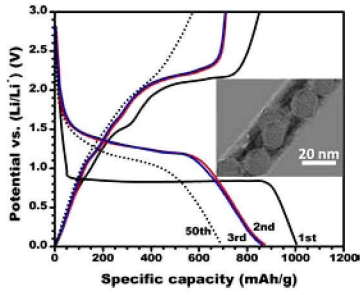

The porous CuNiO/CNT nanocomposite synthesized via a modified co-precipitation method in combination with subsequent-calcination was appliedin the negative electrode materials for lithium-ion batteries and exhibited high electrochemical performance.

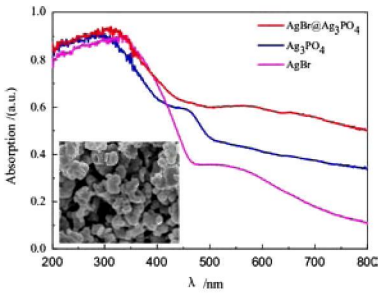

The optical absorption and structural morphology of the as-prepared $AgBr@Ag_3PO_4$ photocatalyst using an anion-exchange precipitation method are conductive to the photocatalytic degradation of organics in water.

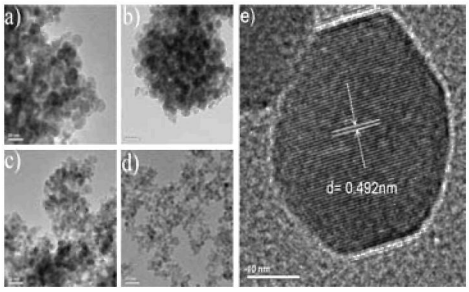

The comparison of the particle size of Mn_3O_4 nanoparticles synthesized using different solvents and HRTEM image of Mn_3O_4 individual nanoparticle revealed its single-crystal nature.

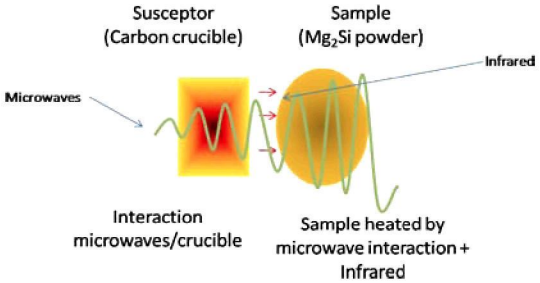

Schematic representation of microwave hybrid heating.

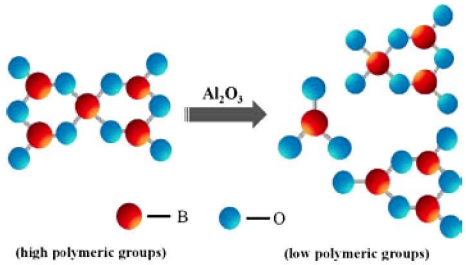

A novel europium valence reduction phenomenon occurred in Al_2O_3 modified borate glasses, FTIR and Raman measurements revealed that high polymeric groups were destroyed to low polymery structures with Al_2O_3 addition.

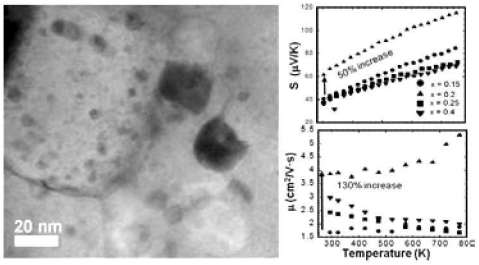

CoSb nanoinclusions embedded into a p-type $Zr_{0.5}Hf_{0.5}Co_{0.4}Rh_{0.6}$ $Sb_{1-x}Sn_x$ half-Heusler matrix simultaneously boost the thermopower and carrier mobility leading to a drastic enhancement of the power factor of the resulting bulk nanostructured materials.

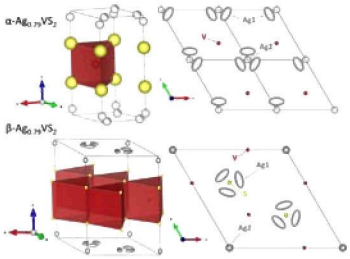

Red = Vanadium, Gray = Silver, Yellow = Sulfur. Top left is α-$Ag_{0.79}VS_2$ in the 1s-$InTaS_2$ structure type. Top right: $2a \times 2b$ projection down the c-axis with displacement ellipsoids (50% probability) of atoms drawn to illustrate the split silver model. Bottom left is β-$Ag_{0.79}VS_2$ having the $a_o\sqrt{(3)}$ supercell. Bottom right: projection along the c-axis, displacement ellipsoids of atoms drawn.

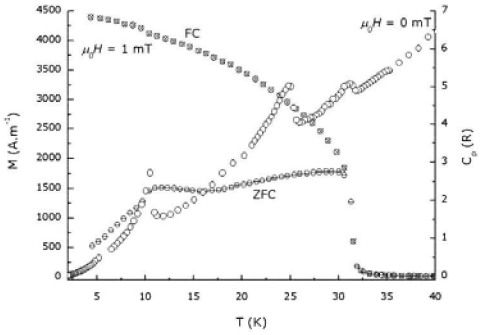

Three ferromagnetic-like phase transitions discovered in the new compound $PbFe_3O(PO_4)_3$ by specific heat and ZFC/FC magnetization measurements.

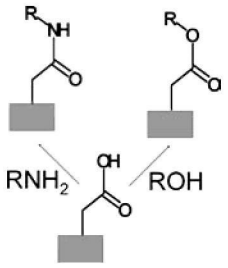

Ester and amide derivatives of layered titanium carboxymethylphosphonate were prepared by solvothermal treatment of amorphous solid with alkanol or alkylamine.

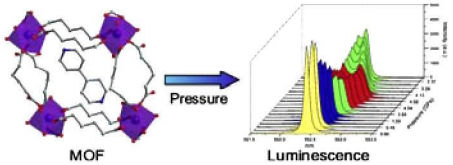

The influence of pressure on the structure and photoluminescence emissions of a 3D terbium-adipate framework.

Continued

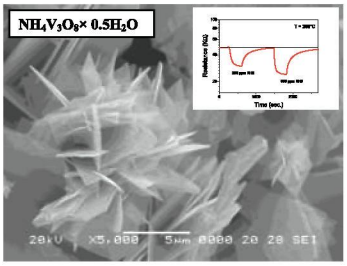

Sheet-like morphology of the synthesized trivanadate hemihydrate ($NH_4V_3O_8 \times 0.5H_2O$). Inset: Its electrical response to different ammonia concentrations in air.

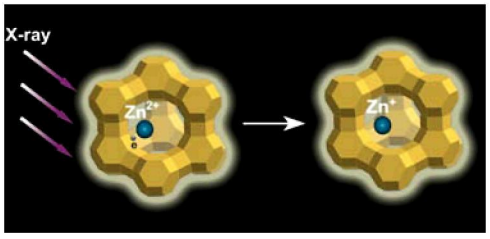

The chemical environment of the zinc species in an electorn-rich zeolite has been elucidated on the basis of X-ray absorption spectroscopy.

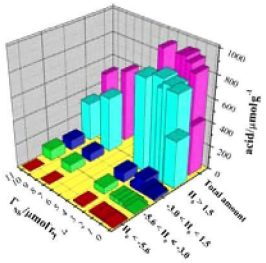

The acid amount and strength of Nb_2O_5/SiO_2 samples varied with the increase of Nb_2O_5 loading. The catalytic activities of the as-prepared samples for the condensation and their acid properties were strongly affected by the dispersion states.

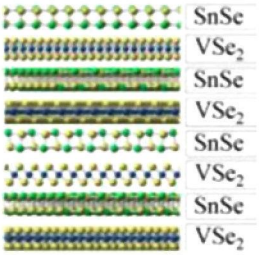

Turbostratically disordered $(SnSe)_{1.15}VSe_2$.

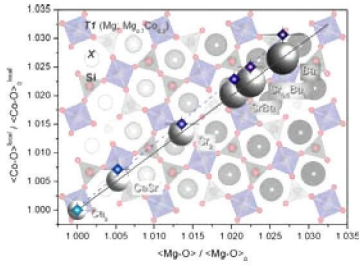

Average (MgO) vs. local (CoO_{local}) tetrahedral bond distances in function of the average *X* cation radius in the $(Ca,Sr,Ba)_2(Mg_{0.7}Co_{0.3})Si_2O_7$ join.

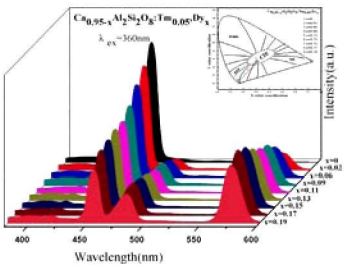

The results indicate the existence of energy transfer from Tm^{3+} to Dy^{3+}. By tuning the concentration of Dy^{3+}, single-phased white light can be realized.

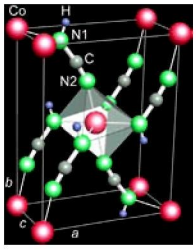

The magnetic ground state of $Co(NCNH)_2$ has been clarified by (spin-polarized) neutron diffraction data at low temperatures. Intensity changes below 4 K arise due to the onset of ferromagnetic ordering of the Co^{2+} spins parallel to the *c* axis, corroborated by various (magnetic) Rietveld refinements.

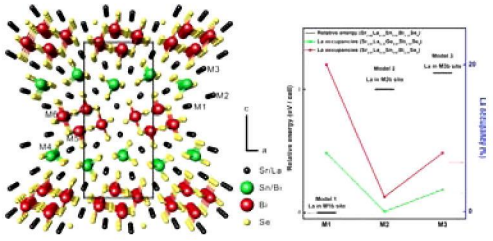

Quinternary selenides $Ae_{2.67}M_{0.33}Tt_{0.67}Pn_{2.33}Se_8$ (*Ae*, *M*, *Tt*, *Pn* = Sr/Ba, Y/La, Ge/Sn, Sb/Bi) were synthesized and their site preferences were characterized by single-crystal X-?ray diffraction and electronic structure calculation.

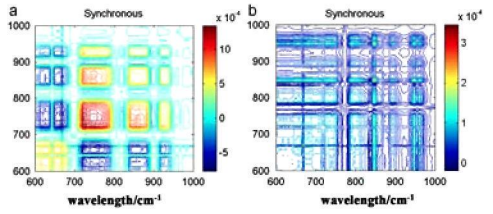

The magnetic-dependent synchronous 2D correlation IR spectra of **1** (a), **2** (b) over 0–50 mT in the range of 600–1000 cm^{-1}, the obvious response indicate two Keggin polyanions skeleton susceptible to applied magnetic field.

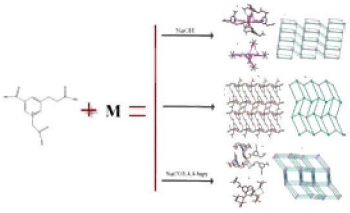

The structural differences show that the ligand, the metal center, and the reaction conditions have great influence on the structure of the final assembly.

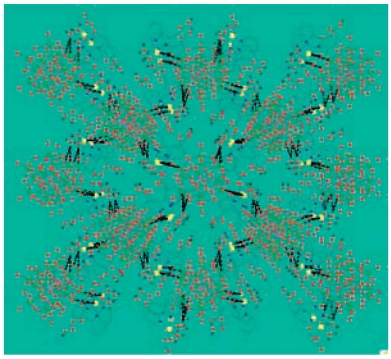

A POM–MOF composite constructed by Keggin-type polyanion, Ni^{2+} and H_2bpdc shows good proton conductivities of 10^{-4}–10^{-3} S cm^{-1} at 100 °C under 3598% RH.

Continued

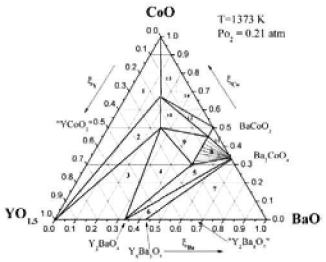

A projection of isobaric isothermal phase diagram of the Y–Ba–Co–O system to the metallic components triangle ($T = 1373$ K, $Po_2 = 0.21$ atm).

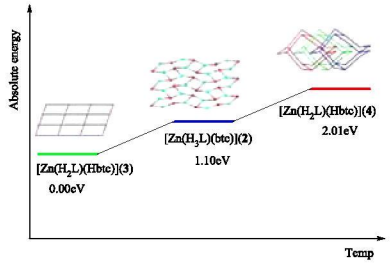

Seven new coordination polymers with multicarboxylate and rigid ditopic 4-imidazole containing ligands have been obtained and found to show different structures and topologies.

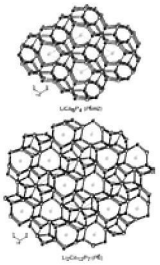

The cobalt–phosphorus networks in $LiCo_6P_4$ and $Li_2Co_{12}P_7$.

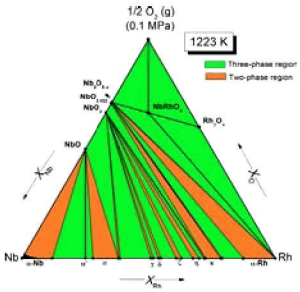

Isothermal section of ternary phase diagram for the system Nb–Rh–O at 1223 K.

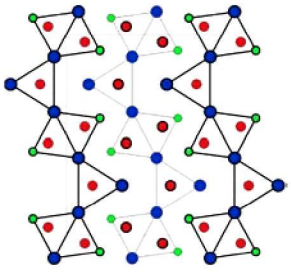

$RE_3M_2Ge_3$ (M = Ru, Ir) adopts the $Hf_3Ni_2Si_3$-type structure containing slabs built up from Ge-centred trigonal prisms.

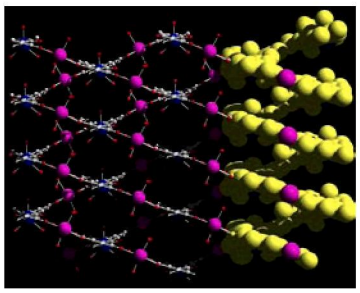

Solvothermal reactions of tricarboxylate ligand H_3L with Cd^{2+}/Ln^{3+} has yielded a series of new MOFs containing interesting structural motifs.

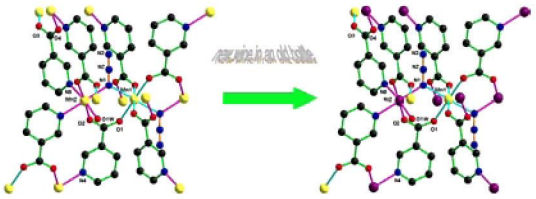

A novel heterometallic 3D complex $[Ni_2Mn(N_3)_2(nic)_4 \cdot (H_2O)_2]_n$ (1) (nic = nicotinate) was synthesized by hydrothermal reaction. This complex exhibits interesting structural and magnetic properties.

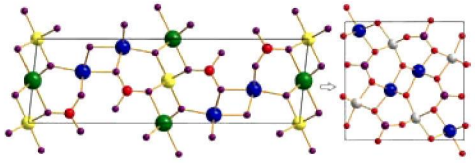

The structural transformation from the monoclinic $MgIn_{7/8}B_{7/8}O_{29/8}$ ($P12_1/n1$) to the orthorhombic $MgInBO_4$ (*Pnma*).

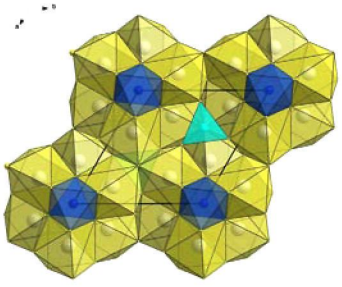

Ln$_3$FeGaQ$_7$ adopt a three-dimensional framework composed of *Ln*Q$_7$ monocapped trigonal prisms with interesting $^1_\infty[FeS_3]^{4-}$ chains and isolated GaQ$_4$ tetrahedra lying in two sets of channels in the framework.

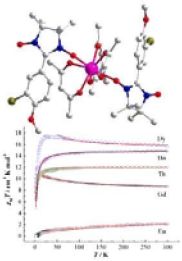

Using a novel halogen phenyl-substituted nitronyl-nitroxide radical, we obtained and characterized five isostructural lanthanide mononuclear tri-spin compounds.

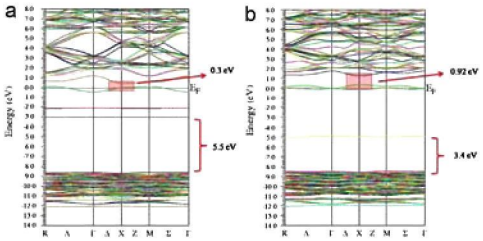

Figure (a) and (b) shows changes in electronic structure and band gap energy of LiF crystal due to presence of Mg and Cu, Mg and P ions respectively.

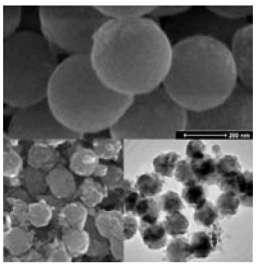

A novel and eco-friendly methodology for the synthesis of mesoscale solid ZnO spheres was developed. The protocol involves a double coating of the starch-derived carbonaceous spheres with successive layers of zinc-containing species by alternating a non-ultrasound and ultrasound-assisted deposition, followed by calcination treatments.

Continued

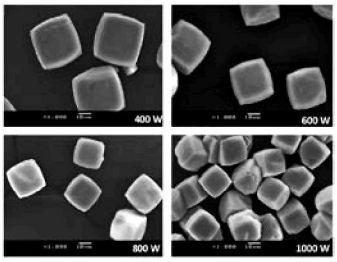

Tailor-made ANA zeolites with varied size can be prepared by simply changing the reaction power.

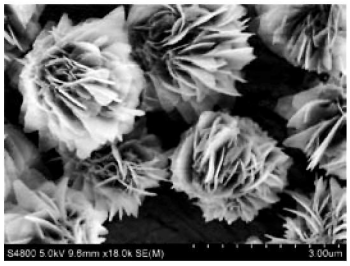

The flower-like γ-AlOOH architectures composed by nanosheets with narrow size distribution (1.6–2.2 μm) and uniform pore size (6.92 nm) have been synthesized via a one-step ionic liquid-assisted hydrothermal route.

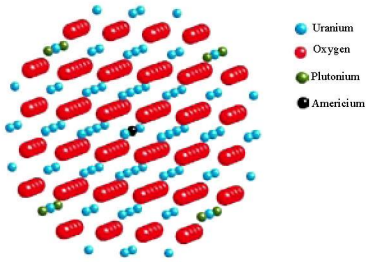

Americium L_{III} XAFS spectra recorded for the irradiated MOX sub-sample in the rim zone for a 300 μm × 300 μm beam size area investigated over six scans of 4 h. The records remain constant during multi-scan. The analysis of the XAFS signal shows that Am is found as trivalent in the UO_2 matrix. This analytical work shall open the door of very challenging analysis (speciation of fission product and actinides) in irradiated nuclear fuels.

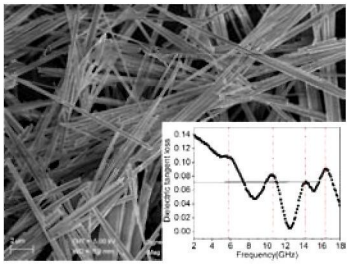

The untralong silver trimolybdate nanowires were synthesized and the dielectric peoperties of the products were studied from 2 to 18 GHz. The as-established equivalent circuit model of the silver molybdate nanowires were employed to explain the nonlinear dielectric resonant behavior.

Rapid Communications

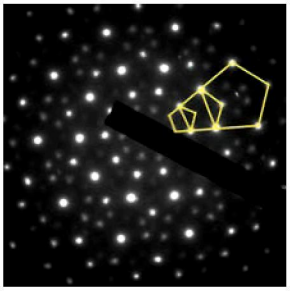

Quasicrystalline Ti–V–Ni–Sc hydrogen storage materials: Sc addition into $Ti_{1.6}V_{0.4}Ni$ alloy forms the icosahedral phase (see picture). With optimal Sc dosage, the anodic cycling stability and self-discharge property are greatly enhanced.

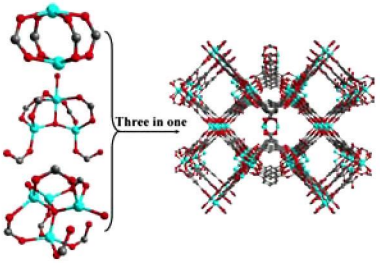

Presented here is a new zinc-1,3,5-benzenetricarboxylate framework integrated three distinct subunits (SBUs).

Synthesis of multi-hierarchical structured yttria-stabilized zirconia powders and their enhanced thermophysical properties

Fengmei Cao, Yanfeng Gao, Hongfei Chen, Xinling Liu, Xiaoping Tang, Hongjie Luo

page 168

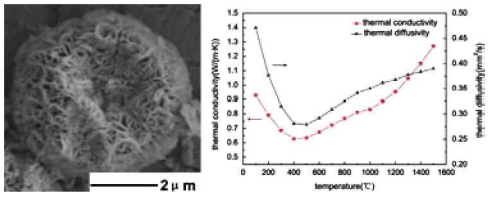

There are many tiny pores and grain boundaries in the multi-hierarchical structured yttria-stabilized zirconia (YSZ) powders, which greatly decrease the thermal conductivities of the YSZ powders.